ZIF-8 derived iron-, sulphur-, and nitrogen-doped catalysts for anionexchange membrane fuel cell application

Iris Palm, Roberta Sibul, Elo Kibena-Põldsepp, Marek Mooste, Jaana Lilloja, Maike Käärik, Jekaterina Kozlova, Arvo Kikas, Alexey Treshchalov, Jaan Leis, et al.

▶ To cite this version:

Iris Palm, Roberta Sibul, Elo Kibena-Põldsepp, Marek Mooste, Jaana Lilloja, et al.. ZIF-8 derived iron-, sulphur-, and nitrogen-doped catalysts for anionexchange membrane fuel cell application. Renewable Energy, 2024, 228, pp.120613. 10.1016/j.renene.2024.120613 . hal-04740666

HAL Id: hal-04740666
https://hal.science/hal-04740666v1

Submitted on 16 Oct 2024

ZIF-8 derived iron-, sulphur-, and nitrogen-doped catalysts for anion-exchange membrane fuel cell application

Iris Palm[a], Roberta Sibul[a], Elo Kibena-Põldsepp[a], Marek Mooste[a], Jaana Lilloja[a], Maike Käärik[a], Jekaterina Kozlova[b], Arvo Kikas[b], Alexey Treshchalov[b], Jaan Leis[a], Vambola Kisand[b], Aile Tamm[b], Nicolas Bibent[c], Frédéric Jaouen[c], Steven Holdcroft[d], Kaido Tammeveski[a,*]
[a]*Institute of Chemistry, University of Tartu, Ravila 14a, 50411 Tartu, Estonia*
[b]*Institute of Physics, University of Tartu, W. Ostwald Str. 1, 50411 Tartu, Estonia*
[c]*ICGM, Univ. Montpellier, CNRS, ENSCM, Montpellier, France*
[d]*Department of Chemistry, Simon Fraser University, 8888 University Drive, Burnaby, BC, V5A 1S6, Canada*

Abstract

This study presents the preparation of tridoped Fe, N, S carbon-based catalysts using ZIF-8 as the main carbon source and iron(II)acetate, 1,10-phenanthroline, ammonia gas and thiourea as precursors for Fe, N and S elements. Thiourea was mixed via planetary ball milling with a Fe-N-C catalyst prepared via inert gas pyrolysis, and different pyrolysis conditions were applied thereafter. The main goal of the work is to synthesise active non-precious metal electrocatalysts for the oxygen reduction reaction (ORR). High electrocatalytic ORR activity in alkaline media was observed for the two materials obtained after thiourea addition and subsequent pyrolysis, while the catalyst resulting from the simple addition of thiourea was less active. Physico-chemical characterisation revealed successful S and N doping for all three catalyst materials with enhanced porosity for the two materials that were subjected to additional pyrolysis after the thiourea addition. The sulphur doping was highest for the FeNSC3 material that was subjected to a second pyrolysis in N_2 and a third pyrolysis in NH_3, compared to the FeNSC2 material that was subjected to a single pyrolysis in NH_3 flow after thiourea addition. The ORR activity of the FeNSC2 catalyst with half-wave potential of 0.88 V vs. RHE was slightly higher than that of FeNSC3, and the former was selected for evaluation as a cathode catalyst in an anion-exchange membrane fuel cell (AEMFC).

---

[*] Corresponding author. Tel.: +372 7375168. E-mail: kaido.tammeveski@ut.ee (K. Tammeveski).

Keywords: anion-exchange membrane fuel cell, ZIF-8, oxygen reduction reaction, electrocatalysis, non-precious metal catalyst, M-N-C catalyst

1. Introduction

The growing population and therefore increasing energy consumption alongside with global warming has led to searching and developing of more environmentally friendly energy sources for both stationary and transportation applications. One of the promising solutions for this problem is using hydrogen as a fuel for producing electricity. In order to convert the chemical energy of hydrogen into electrical energy, fuel cells are needed [1–3]. Fuel cell are clean and sustainable energy conversion devices attracting increasing attention in the transition to hydrogen economy [4]. Green hydrogen is produced by water electrolysis using renewable energy sources (solar, wind, hydropower) and is used then as a fuel in a fuel cell. There are two types of low temperature fuel cells: proton-exchange membrane fuel cells (PEMFC) and anion-exchange membrane fuel cells (AEMFC). While PEMFC is a mature technology that has been employed in several sectors, recent progress in the field of AEMFC development has made these devices very promising for various applications [5]. The main advantage of AEMFCs is the possibility of using Pt-free cathode catalysts due to less harsh conditions. In both devices, the two main reactions taking place are hydrogen oxidation reaction at the anode and oxygen reduction reaction (ORR) at the cathode [6]. The four-electron ORR is sluggish in both AEM and PEM environments and makes it one of the main obstacles in fuel cell technology [6,7]. Pt or Pt-alloy based materials are widely used as electrocatalysts for low-temperature fuel cells to catalyse the ORR [8–10]. Yet, recent progress in non-precious metal catalysts brings hope that such materials might replace precious metal-containing catalysts, the latter having the drawbacks of being expensive and with limited resource [11–14].

Non-precious metal ORR catalysts are typically divided into two main groups: (i) metal-free and (ii) transition metal-containing nanocarbons. Carbon materials can be activated for ORR electrocatalysis by doping it with different heteroatoms, such as nitrogen, sulphur, boron or phosphorus, or a combination of these dopants [15–21]. Such materials have limited ORR activity in acid medium but can reach significant ORR activity in alkaline medium. The second group of materials features a non-precious transition metal, most often iron or cobalt, embedded in a carbon matrix in combination with nitrogen groups acting as ligands of the metal cations [13,22–29]. Beside stabilizing the metal cations through strong metal-N coordination, it is known that nitrogen doping also leads to a synergistic effect between carbon and nitrogen atom, the nitrogen's lone electron pairs being able to form a delocalised conjugated system sp^2 hybridised carbon frameworks. This improves greatly the reactivity and ORR performance of the material [20,21,30,31]. In case of co-doping carbon with sulphur and nitrogen, there has also been observed an increase in the ORR activity due to increased number of active sites and synergetic effect between the two dopants [17,20,21,32–34]. Using iron alongside with nitrogen for doping graphene-based materials has been widely studied [24,25,35,36]. These materials are highly conductive, relatively chemically stable and can be tailored to have high surface areas. The nature of the transition metal in these catalyst materials plays a great role in the formation of active sites for ORR [37–43]. The general idea is that the increase in the ORR electrocatalytic activity can be assigned to either Fe-N_x coordination sites or to iron carbide or metallic iron particles, which are embedded in nitrogen-doped graphitic layers [44–47].

Metal organic frameworks (MOFs), a class of crystalline materials constructed by the coordination of metal ions or clusters and organic bridging ligands in three dimensional space, have been used as sacrificial materials since 2011 to prepare via high-temperature pyrolysis highly active precious-metal-free ORR electrocatalysts [48–53]. Some MOFs have high porosity and high specific surface area (up to 6200 m^2 g^{-1}) compared to other porous materials [54–57], and can lead to carbon-based materials also with high porosity and high pore connectivity, after pyrolysis. Zeolitic imidazolate frameworks (ZIFs) is a sub-class of MOFs, which possess the topology of zeolites but are composed of imidazolate groups coordinating either Zn(II) or Co(II) [58]. One of the well-known ZIFs is ZIF-8 which is composed of $Zn(MeIm)_2$ primary units (Zn ions and 2-methylimidazolate linkers) and has a sodalite-type structure [59]. ZIF-8 has hitherto been the main MOF used to form highly active ORR catalysts via pyrolysis, due to the intrinsic properties of ZIF-8 like high surface area, high nitrogen content and high microporosity combined with facile synthesis as well as controllable ZIF-8 crystal size [50,54,60–63].

Dominant research activity in the field of ORR electrocatalysis has focused on the preparation of non-precious metal catalysts and methodological evaluation of the electrocatalytic properties of these catalysts in the rotating disc electrode (RDE) setup. Much less research effort has been put on evaluating such catalysts in fuel cell environment, using these electrocatalysts as cathode materials. PEM fuel cell testing of precious metal free cathode catalysts is becoming more popular, eased by the availability of highly conductive and robust commercial PEM membranes and ionomers. However, the ORR on precious-metal-free catalysts has often faster kinetics in alkaline conditions compared to acidic media, so there has been a shift towards the research in AEM fuel cells since the advent of AEM with promising conductivity [64].

Although numerous synthesises have been reported using ZIF-8 as a sacrificial MOF for the preparation of carbon nanomaterials co-doped with a transition metal (most often Fe or Co) and a non-metal heterogeneous element (most often N, but also, P, S), however the majority of the catalysts that have been investigated in fuel cell environment are the Fe-N-C and Co-N-C materials, and the overwhelming majority of fuel cell studies involving such materials have been carried out in PEMFC environment [26,54,62,63,65]. In particular, the study of materials with co-doping of N and S hetero-elements has not yet been reported in fuel cell environment. In this work, tri-doped Fe, N and S carbon-based catalysts were synthesised using ZIF-8 as the main carbon precursor, and applying a facile low energy ball-milling method to introduce the sulphur dopant, namely thiourea. This was optionally followed by one or two high-temperature pyrolysis, in order to covalently introduce S in the carbon matrix as well as to re-open pores blocked by thiourea addition. The obtained materials were electrochemically characterised using the RRDE method followed by testing in AEM fuel cell configuration. The physico-chemical characterisation of the catalysts was performed using scanning electron microscopy (SEM) to describe the morphology of the catalysts, X-ray photoelectron spectroscopy (XPS) to determine the elemental composition of the surface of the catalysts, X-ray diffraction (XRD) to identify the crystalline phases present, and N_2 adsorption/desorption analysis for determining the surface area and porosity of the catalysts.

2. Material and methods

2.1 Synthesis procedure of the ZIF-8 based Fe,S,N-doped catalysts

To synthesise the catalysts, ZIF-8 (Basolite Z1200, Sigma-Aldrich) was used as the main carbon source, iron(II)acetate ($Fe(OAc)_2$, ≥99.99%, Sigma-Aldrich) as an iron source, 1,10-phenanthroline (phen, ≥99.99%, Sigma-Aldrich) as nitrogen source and thiourea (≥99.99%, Sigma-Aldrich) as a dual sulphur and nitrogen precursor. ZIF-8, $Fe(OAc)_2$ and phen were first weighed (see Table 1), mixed via ball-milling (FRITSCH Pulverisette 7 Premium) in dry conditions using 5 mm size ZrO_2 beads and a jar with ZrO_2 lining, at 400 rpm for 4 × 30 min (with 5 min break between each of the four cycles). Subsequently, the obtained material was ramp heated from room temperature to 1050 °C in N_2 atmosphere with a ramp rate of 5 °C min^{-1}, held at that temperature for 1 h. Afterwards, thiourea was added to the pyrolysed material and mixed with the same ball-miller but applying a low rotation speed of 100 rpm for 10 min (see Scheme 1). The prepared catalyst is designated as FeNSC1. To potentially improve the ORR activity, an ammonia treatment was applied to FeNSC1, and the obtained catalyst material was flash pyrolyzed at 950 °C in flowing NH_3 atmosphere for 5 min. The resulting catalyst is designated as FeNSC2 (Scheme 1). A third synthesis was also conducted, sharing the same initial steps as for FeNSC1 but differing in the final pyrolysis step after thiourea addition. Namely, after ball milling of the pyrolyzed material with thiourea, the material was flash pyrolyzed at 800 °C in N_2 atmosphere for 20 min directly followed by ammonia treatment for 5 min at 950 °C (see Scheme 1). The resulting catalyst is designated as FeNSC3. The key idea for performing first a pyrolysis at 800° C in N_2 after thiourea addition is to covalently integrate the sulphur in the carbon matrix, before applying the more aggressive NH_3 pyrolysis.

Table 1. Synthesis conditions for the N, S co-doped FeNSC1 catalyst

Catalyst	**ZIF-8 (mg)**	**phen (mg)**	**$Fe(OAc)_2$ (mg)**	**Thiourea (mg)**
FeNSC1	800	100	15.7	¼ of the mass of material remaining after the pyrolysis at 1050 °C

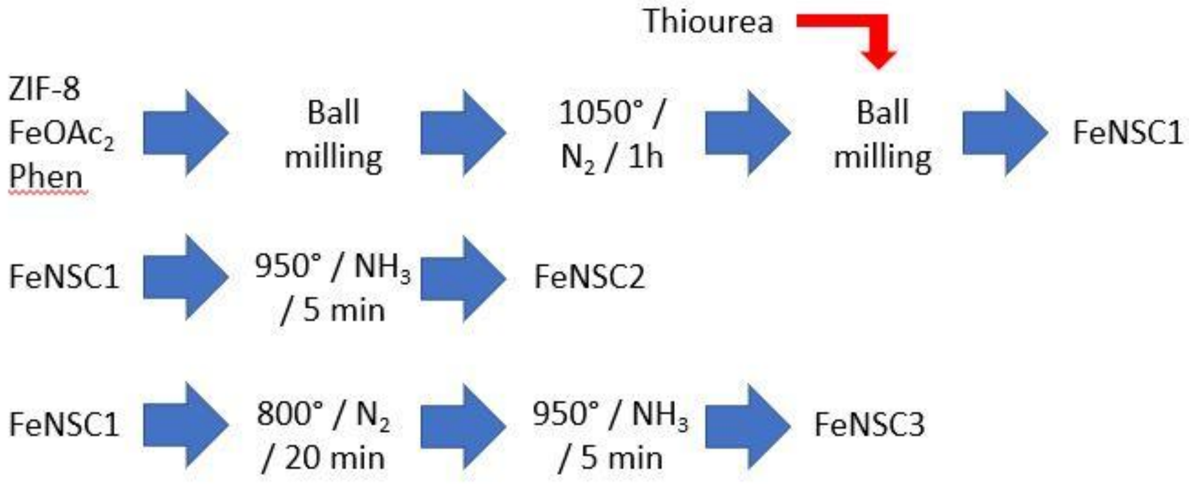

Scheme 1. Scheme of the synthesis approaches.

2.2 Physico-chemical characterisation

Helios Nanolab 600 (Thermo Fisher Scientific (former FEI) scanning electron microscope (SEM) was used to investigate the morphology of the prepared catalysts. The elemental composition was investigated with XPS analysis using an electron energy analyzer SCIENTA SES-100 and Mg K_a radiation (1253.6 eV) from nonmonochromatic twin anode X-ray tube Thermo XR3E2. The XPS data analysis involved removal of X-ray satellites, peak fitting (using the Gauss-Lorentz hybrid functions and blend of linear and Shirley type backgrounds) and calculation of atomic concentrations. N_2 adsorption/desorption isotherms of the catalysts were recorded at 77 K using a NovaTouch LX2 analyser (Quantachorme). The specific surface area (S_{DFT}) and pore size distribution (PSD) and the volume of micropores (V_{micro}) of the obtained catalyst materials were calculated by the Quantachrome software, using the quenched solid density functional theory (QSDFT) method (with the kernel for N_2 at 77 K on carbon, slit pore, equilibrium model, desorption data). The specific surface area ($\mathrm{SSA}_{\mathrm{BET}}$) was calculated using the Brunauer-Emmett-Teller theory in the pressure range up to P/P_0=0.2. The total pore volume (V_{tot}) was measured at P/P_0=0.97. Raman spectroscopy was used to characterise the carbon matrix in these catalyst materials. All samples were suspended in water and drop-coated on silicon substrates. Micro-Raman spectra were recorded in the back-scattering geometry on an inVia Renishaw spectrometer in conjunction with a confocal microscope (Leica Microsystems CMS GmbH), 50X objective and an argon ion laser operated at 514.5 nm. Low incident laser power density at the sample prevented excessive sample heating and/or decomposition, while allowing getting averaged information over ~200 μm^2 area in a single exposure.

X-ray diffraction (XRD) patterns were acquired with a X'Pert MPD instrument equipped with a θ- θ goniometer, in Bragg Brentano geometry and using the Cu $K\alpha_1$ radiation. The instrument was also equipped with a sample holder of spinner type and with a linear detector

X'Celerator. Diffractograms were recorded in the 2θ interval from 5 to 90° with a step of 0.0167°, during a total of 4 h for each spectrum. For powder XRD measurements on the different materials, either a polyimide film was placed on top of the powder and the powder placed on a glass support, or no cover film was used but a PTFE support was used. The XRD signal of the supports alone and of the polyimide cover film alone were also acquired.

2.3 Rotating ring-disk electrode measurements

The ORR activity of the catalyst materials was evaluated by the RRDE method where glassy carbon disk (GC, geometric area of 0.164 cm^2) with Pt ring (collection efficiency of 0.22) was used as a working electrode, saturated calomel electrode (SCE) as a reference electrode and platinum wire as a counter electrode. All the electrochemical potentials are reported with respect to the reversible hydrogen electrode (RHE). Potential values are converted from versus SCE to versus RHE in 0.1 M KOH using the equation: $E_{\mathrm{RHE}} = E_{\mathrm{SCE}} + 0.241 + 0.059 \times \mathrm{pH} = E_{\mathrm{SCE}} + 1.008$ V. The potential was controlled by Autolab potentiostat/galvanostat PGSTAT30 (Metrohm Autolab, The Netherlands) using General Purpose Electrochemical System (GPES) software. All the measurements were carried out in 0.1 M KOH electrolyte at the electrode rotation rate (ω) of 1600 rpm and at the potential scan rate (v) of 10 mV s^{-1}. The data acquired in O_2-saturated electrolyte was corrected for the data acquired in N_2-saturated electrolyte, to obtain the Faradaic polarisation curves. The number of electrons (n) transferred per O_2 molecule was determined from the RRDE data using Eq. (1)

$$n = \frac{4I_{\mathrm{d}}}{I_{\mathrm{d}} + \frac{I_{\mathrm{r}}}{N}} \tag{1}$$

and the percentage yield of HO_2^- formation (%HO_2^-) was calculated via the Eq. (2):

$$\%\mathrm{HO}_2^- = \frac{\frac{2I_{\mathrm{r}}}{N}}{I_{\mathrm{d}} + \frac{I_{\mathrm{r}}}{N}} \times 100\% \tag{2}$$

where I_d is the disc current, I_r is the ring current, and N is the collection efficiency of the Pt ring.

To prepare the FeNSC catalyst inks for coating the GC electrode, 4 mg of catalyst material was dispersed in a mixture of 990 µL of 2-propanol and 40 µL of Nafion solution (5 wt % of Nafion in solution) and sonicated for 1 h. The obtained catalyst ink was drop cast onto a polished GC surface to reach a loading of 0.2 mg cm^{-2}. For comparison, the GC electrode was modified with a Pt/C catalyst (20% wt%, E-TEK) using the same procedure as for the FeNSC catalysts, also resulting in a Pt/C loading of 0.2 mg cm^{-2}.

The electrochemical stability of the FeNSC catalysts was tested in O_2-saturated 0.1 M KOH solution by applying 10000 potential cycles between 0.6 and 1.0 V vs. RHE at 200 mV s^{-1}.

2.4 Anion-exchange membrane fuel cell (AEMFC) tests

Fuel cell measurements were carried out using Greenlight Fuel Cell Test Station (G40 Fuel Cell System, Hydrogenics, Canada). To prepare the cathode, 12.5 mg of the catalyst material (FeNSC2) was dispersed in a solution, which contained 1340 µL methanol (99.5%, Fisher Scientific), 391 µL Milli-Q water and 130 µL 3 wt.% ionomer solution prepared by dissolving methylated poly[2,2′-(2,2″,4,4″,6,6″-hexamethyl-p-terphenyl-3,3″-diyl)-5,5′-bibenzimidazole] membrane (iodide form [66]) in methanol. For preparing the anode electrode for the fuel cell, 6.7 mg of Pt–Ru/C catalyst (50:25:25, Alfa Aesar) was dispersed in a solution of 689 µL methanol, 196 µL Milli-Q water and 49 µL 3 wt.% ionomer solution in methanol (Aemion+ powder (AP2-INN8-00-X) (Ionomr Innovations, Inc., Canada). The obtained suspensions were sonicated for 1.5 h and pipetted onto the gas diffusion layer (GDL, Sigracet 39 BB) giving a final loading of 2 mg cm^{-2} for cathode and 0.8 mg$_{\text{Pt-Ru}}$ cm^{-2} for anode. Before testing, the electrodes were soaked in 3 M KOH for one day and the AEM for four days. The 3 M KOH solution for ionic exchange in AEM was changed after every 24 h. The prepared anode and cathode were pressed together into a 5 cm^2 test cell (Fuel Cell Technologies Inc., Albuquerque, USA) along with a reinforced AEM (Aemion+ AF2-HLE8-10-X, 10 µm from Ionomr Innovations Inc., Canada) with silicone gaskets at a torque of 9 Nm. The single-cell tests were carried out at 65 °C with 75% relative humidity, O_2 and H_2 flow rates were both 0.05 NLPM and the backpressure was 200 kPa on each side.

3. Results and discussion

3.1 Physico-chemical characterisation of the FeNSC catalysts

To examine the surface morphology of the FeNSC materials scanning electron microscope was used and the SEM micrographs are shown in Fig. 1. As can be seen, all prepared materials have a rough morphology that is composed of irregularly shaped particles ranging in size from a few tens to hundreds of nanometres. The particles are interconnected, providing a porous framework that covers the electrode's surface rather uniformly. According to the N_2 physisorption studies which were conducted to analyse the specific surface area (SSA) and porosity parameters of the obtained FeNSC catalysts confirm that all the materials have highly porous structure (see Table 2).

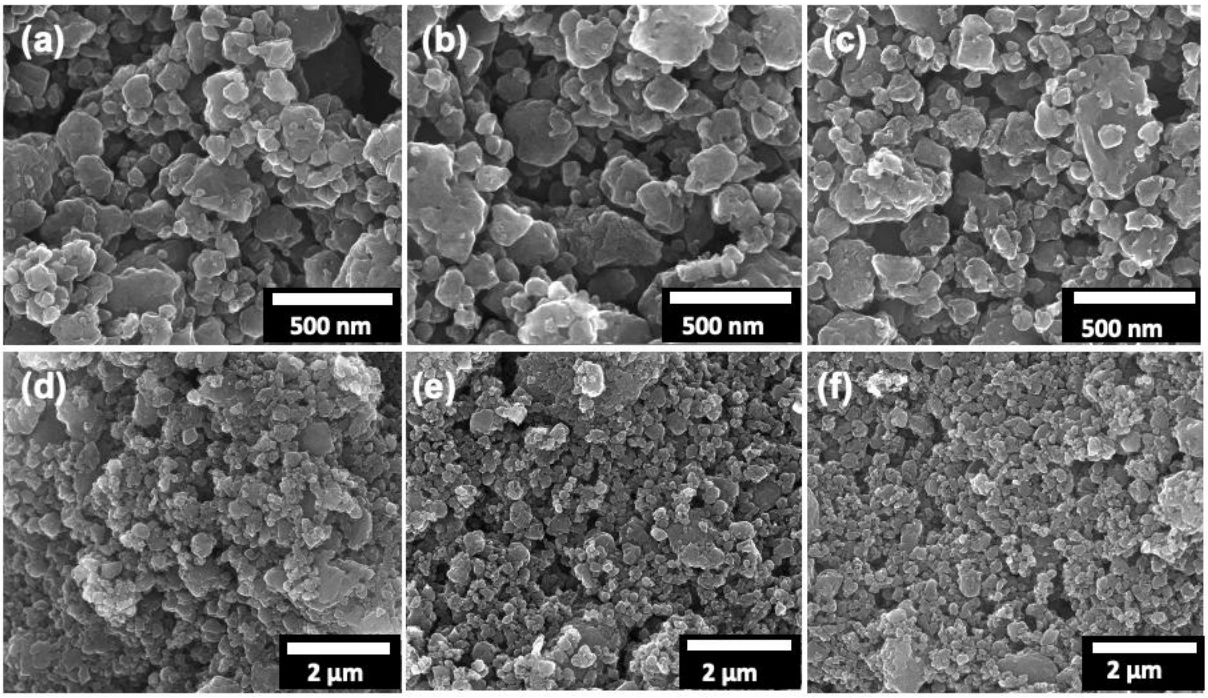

Fig. 1. SEM images of (a,d) FeNSC1, (b,e) FeNSC2 and (c,f) FeNSC3 materials.

As can be seen from the inset of Fig. 2, the shape of N_2 physisorption isotherms are similar for all three catalysts and refers to a mix of type I and type II. At the isotherms of all materials, the presence of a weak H4 type hysteresis loop according to IUPAC can be observed [67]. These results show that all catalysts consist of micro-and mesopores. This is also confirmed by the results of pore size distribution (PSD, Fig. 2). Two distinct peaks were detected at 0.8 nm and 3.5 nm for all three materials, corresponding to the hierarchical (micro- and mesopores) porous structure. However, the PSD shows a more intense signal for the micropores centred at 0.8 nm, which indicates that the surface area of the materials is mostly existing in micropores rather than mesopores (see Fig. 2), also reflected in the values of $SSA_{micro(dft)}$ and $SSA_{meso(dft)}$, as seen in Table 2. The difference in the PSD is mostly seen in the pore size region from 1 to 2 nm, in line with the reported effect that NH_3 pyrolysis generally leads to the formation of micropores by preferential etching of the amorphous carbon phase.

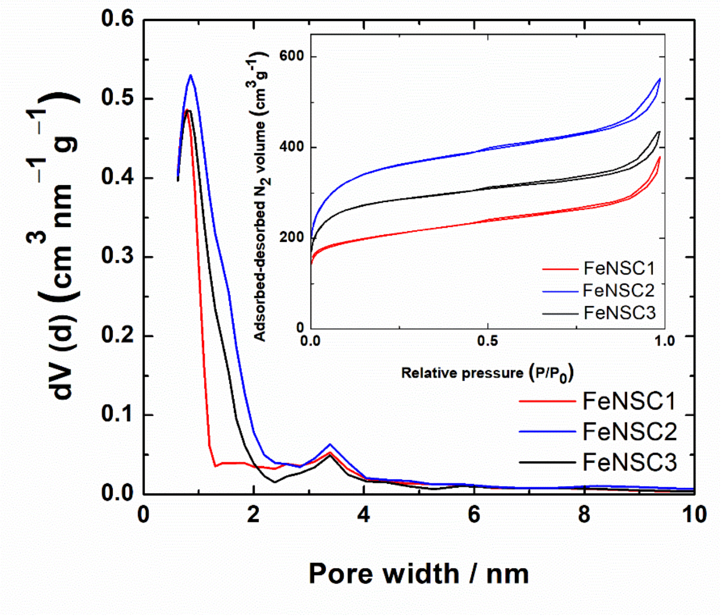

Fig. 2. Pore size distribution of FeNSC materials. The inset exhibits N_2 adsorption-desorption isotherms for all the prepared catalysts.

The highest SSA_{BET} was determined for FeNSC2 (1260 m^2 g^{-1}) followed by FeNSC3 (992 m^2 g^{-1}), whereas FeNSC1 compared to the other two catalysts exhibited significantly lower SSA with the value of 717 m^2 g^{-1}. Higher SSA of FeNSC2 and FeNSC3 vs. FeNSC1 is related to the pyrolysis steps applied after the thiourea addition by ball-milling, and in particular the NH_3 activation step applied to these two materials. These pyrolysis steps after thiourea addition by ball milling can re-open pores that were filled with thiourea in FeNSC1 or create new pores in the carbon matrix existing in FeNSC1. It was reported that NH_3 pyrolysis can react preferentially with the amorphous carbon phase, gasifying it and resulting in the formation of micropores in particular between the more resistant graphitic crystallites, and thus leading to increased pore volume and surface area [68–70]. Larger surface is significant in the electrochemical reaction for faster electron transfer and mass transport [71,72]. The highest pore volumes (V_{tot} and V_{micro}) were obtained for FeNSC2, while the porosity was considerably lower for the other two catalysts (see Table 2).

Table 2. Textural properties of FeNSC catalysts determined by the N_2 physisorption method.

Catalyst	**SSA$_{BET}$** (m^2 g^{-1})	**SSA$_{dft}$** (m^2 g^{-1})	**SSA$_{micro(dft)}$** (m^2 g^{-1})	**SSA$_{meso(dft)}$** (m^2 g^{-1})	**V_{tot}** (cm^3 g^{-1})	**$V_{micro(dft)}$** (cm^3 g^{-1})
FeNSC1	717	767	692	75	0.52	0.27
FeNSC2	1260	1122	1032	90	0.78	0.49
FeNSC3	992	942	881	61	0.61	0.39

X-ray photoelectron spectroscopy analysis was carried out to investigate surface composition of the catalyst materials. The XPS analysis revealed that the introduction of iron as well as nitrogen and sulphur moieties into the FeNSC catalysts was successful. The XPS survey spectra distinguished five peaks at 285, 535.5, 711, 400 and 167 eV, which were attributed to the binding energies of C1s, O1s, Fe2p, N1s and S2p, respectively (see Fig. 3a,c,e).

For sulphur, relatively low contents are measured for all three samples, and in particular for FeNSC1 (see Table 3). This is counterintuitive as thiourea was milled with the pyrolyzed material resulting from ZIF-8/phen/FeOAc2 pyrolysis, with 20 wt% thiourea added relative to the pyrolyzed material. Thus, the expected bulk S content for FeNSC1 would be ca. 8 at.%, while only 0.01 at.% S is detected. This shows that most of the sulphur is not detected by XPS and this can be interpreted as the packing of thiourea in micropores of the pyrolyzed materials, preventing the S-atoms from thiourea molecules located deep in the micropores to be detected by XPS. This hypothesis is perfectly in line with increased amounts of S detected by XPS in FeNSC2 and FeNSC3, increasing to 0.1 and 0.5 at.%, respectively. For FeNSC3, a first pyrolysis at 800 °C in inert gas was applied after thiourea addition and a final pyrolysis in NH_3 made at 950 °C. This results in a significantly higher S content in the final catalyst, compared to the direct application of an NH_3 pyrolysis after thiourea addition (FeNSC2 synthesis). For the FeNSC3 catalyst, the most intense sulphur-related signal was detected at the binding energies of ~164 and ~165 eV, which correspond to $S2p_{3/2}$ and $S2p_{1/2}$ spin-orbit split components, respectively (Fig. 3e inset). Based on the literature, these peaks belong to thiophene-S (C-S-C) bond. In the case of FeNSC2 (Fig. 3c inset), this sulphur species is absent, and instead there are peaks at ~168 and ~169 eV that can be assigned to oxidised-S groups (SO_x) [73–76]. Oxidised S-groups are present in low amount in FeNSC3 and totally absent in FeNSC1.

The nitrogen content in the three catalyst materials was significantly higher compared to Fe and S, in the range of 6-7 at.% (Table 3). The XPS spectra in the N1s region was deconvoluted into different peaks that identify different N groups (Fig. 3b,d,f). For all three materials, the most prominent ones were pyridinic-N (398.5 eV) and pyrrolic-N (400.6 eV), while peak intensities for imines (397.7 eV), graphitic-N (402 eV) and Fe-Nx (399.5 eV) were lower and comparable among the materials. The Fe-N_x signal is of particular interest for ORR catalysis and FeNSC2 had the highest absolute content of Fe-N_x followed by FeNSC1, while FeNSC3 has significantly lower absolute content of Fe-N_x signal (Table 3). These active centres and different N species play an important role in enhanced ORR performance, as discussed in the next subsection.

The Fe content measured by XPS was the same for all three materials, at 0.3 at.%. This is in line with the Fe content expected, since the Fe content in the ZIF-8/phen mix before pyrolysis is 1.7 wt.%, and ZIF-8 loses typically 66 % of its mass during its first pyrolysis at 1050 °C in inert gas. The O content is in the range of 3.9-4.5 at.% for the three materials, in line with previous reports and assigned to adventitious oxygen, and/or O_2 adsorbed on Fe-N_x sites following exposure of the catalysts to the ambient atmosphere [77].

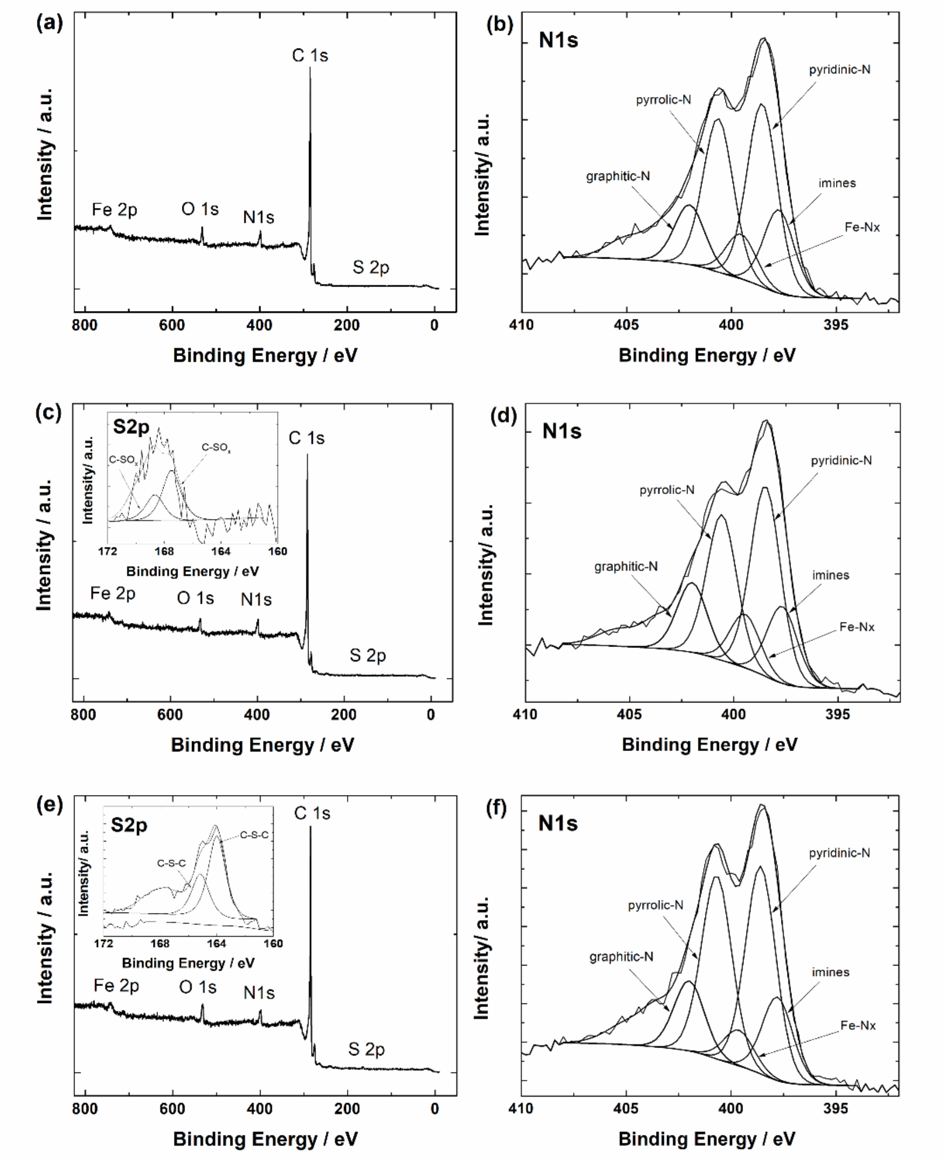

Fig 3. XPS wide scan and detailed N1s spectra of (a,b) FeNSC1, (c,d) FeNSC2 and (e,f) FeNSC3, respectively. Inset to (c) and (e) shows the detailed spectra in the S2p region.

Table 3. Surface elemental composition (at.%) of FeNSC materials measured by XPS, and the absolute content of N subdivided into different N species.

	FeNSC1	**FeNSC2**	**FeNSC3**
C	89.5	88.8	88.7
O	4.2	3.9	4.5
N	6	6.9	6.0
S	0.01	0.1	0.5
Fe	0.3	0.3	0.3
pyridinic-N	1.9	2.2	1.9
pyrrolic-N	1.6	1.7	1.7
imines	0.9	0.9	0.8
graphitic-N	0.6	0.8	0.7
Fe-N$_x$	0.5	0.6	0.3
other N moieties (N-O, N-H etc.)	0.5	0.7	0.6

The three catalysts were investigated with XRD. For interpreting the diffractograms, it is important to recall that FeNSC1 was measured with a polyimide film placed on top of the powder and the powder placed on a glass support, while FeNSC2 and FeNSC3 diffractograms were acquired without any cover film but using a PTFE support, as detailed in the experimental methods. The reference diffraction patterns for the polyimide film, the glass support and the PTFE support are shown in Fig. 4c,e,f, respectively, while the spectra measured for FeNSC1, FeNSC2 and FeNSC3 are shown in Fig. 4a,b,d.

For FeNSC1, the broad peak centred at ca 20.8° and the shoulder at 25.9°can be assigned to the polyimide film. Then, the well-defined XRD peaks at 30.1, 35.07, 50.2, 60.0 and 62.7° can be assigned to tetragonal ZrO_2, matching in positions and in their relative intensities to reference XRD patterns of this phase (JCPDS file 01-079-1769). ZrO_2 impurities must have been introduced during the first ball-milling process at 400 rpm, since the lining of the jar and the balls used to mill are made of ZrO_2. Such ZrO_2 fragments introduced during milling would then have been subjected to the same pyrolysis treatment applied to prepare the catalysts. Literature has shown that tetragonal ZrO_2 is expected after high temperature treatment, since it is the thermodynamically stable zirconium oxide phase at high temperature [78]. The presence of tetragonal ZrO_2 here is also in line with our previous publication on the preparation of Fe-N-C materials from carbide derived carbons via milling in ZrO_2-lined jar and with ZrO_2 balls, where the main signal was from tetragonal ZrO_2 and a minor signal from hexagonal ZrO_2 [23]. Next, the broad peak centred at 43.5° can be assigned to the (101) diffraction line of graphite, and indicates the amorphous nature of the carbon matrix in FeNSC1.

All the well-defined peaks observed in the XRD pattern of FeNSC2 can be assigned to the PTFE support used for acquisition of that diffractogram, except the peaks located at 30.28° and 44.93°. The former can be assigned to the most intense diffraction peak of tetragonal

ZrO_2, while secondary diffraction peaks of this phase are not detected, suggesting a lower amount of ZrO_2 in FeNSC2 than in FeNSC1. The peak at 44.93° can be assigned to the main diffraction peak of α-Fe. The secondary diffraction peaks of α-Fe are also not visible in the XRD pattern, which is typical in FeNC materials due to low absolute Fe amount, with nanometric metallic Fe particle size. Moreover, α-Fe only accounts for part of the iron, the remainder being present as atomically dispersed Fe-N_x sites. Last, the broad peak centred at ca 42° and extending from 35-47° may be due to the amorphous carbon phase in FeNSC2, and/or may be due to the PTFE support since the latter also shows a broad background in that angle region (see Fig. 4f). All the well-defined peaks observed in the XRD pattern of FeNSC3 can be assigned to the PTFE support used for acquisition of that diffractogram. As for FeNSC2, the broad peak centred at ca 42° and extending from 35-47° may be due to the amorphous carbon phase in FeNSC3, and/or may be due to the PTFE support.

Overall, the absence of peaks related to iron-based crystalline phases in FeNSC1 and FeNSC3 suggests that all or the vast majority of iron is present as atomically dispersed iron sites in these materials, while FeNSC2 contains some metallic α-Fe. The presence of some α-Fe in FeNSC2 but absence in FeNSC3 may be assigned to the synthesis path, FeNSC2 being prepared by applying a pyrolysis in flowing ammonia at 950 °C to the milled thiourea and FeNSC1 mix, corresponding to highly reducing conditions (see the synthesis Scheme). In contrast, FeNSC1 was only pyrolyzed in N_2 gas, while FeNSC3 is derived from the milled thiourea and FeNSC1 mix by applying first a pyrolysis at 800 °C in N_2 gas, followed by another pyrolysis in flowing ammonia at 950 °C. The combination of thiourea and NH_3 during a pyrolysis stage therefore seems to explain the presence of some α-Fe in FeNSC2.

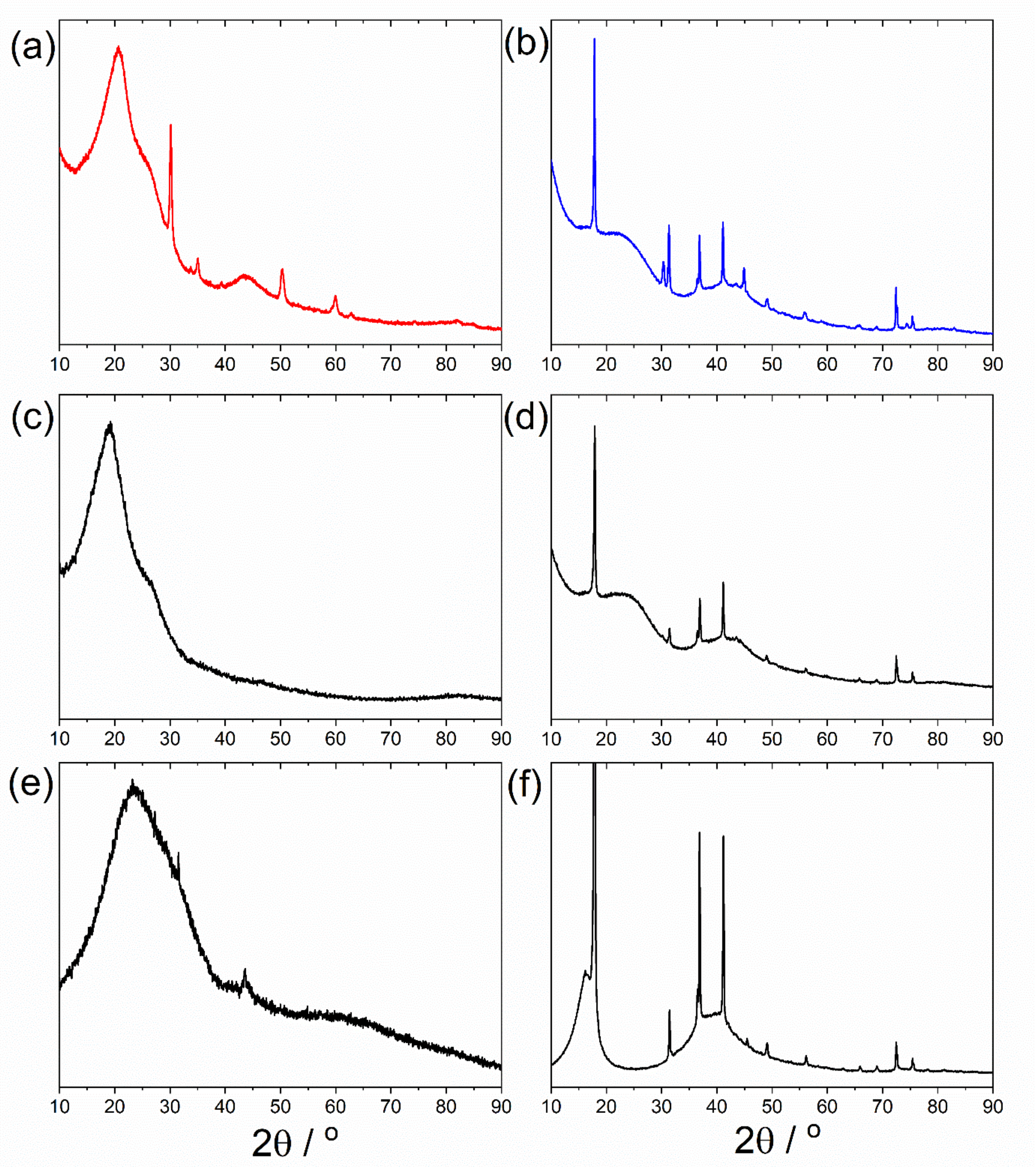

Fig. 4. XRD patterns of the catalysts and films or supports used to acquire the data. (a) FeNSC1, (b) FeNSC2, (c) polyimide film, (d) FeNSC3, (e) glass support and (f) PTFE film.

The first-order Raman spectra of the catalysts normalized to the intensity of the G band are presented in Fig. 5. The spectra were fitted following the four-peak model where G peak (~1590 cm^{-1}) corresponds to the stretching vibrations of the sp^2 carbon atoms in the ideal graphitic lattice; D1 (~1350 cm^{-1}) to defect-activated breathing mode of aromatic rings; D3

(~1500 cm^{-1}) to amorphous carbon and D4 (~1150 cm^{-1}) to disordered graphitic lattice [79]. A baseline correction was used to compensate for the small fluorescence background and multiple-peak fitting procedure was applied using the PeakAnalyser software in OriginPro 9. The intensities of I_{D1} and I_G (integrated areas under the bands) were extracted from the fitting of the curves by Voigt functions. In the curve-fitting procedure, all parameters (peak position, height, and width) were adjusted to attain the smallest value of the chi-square.

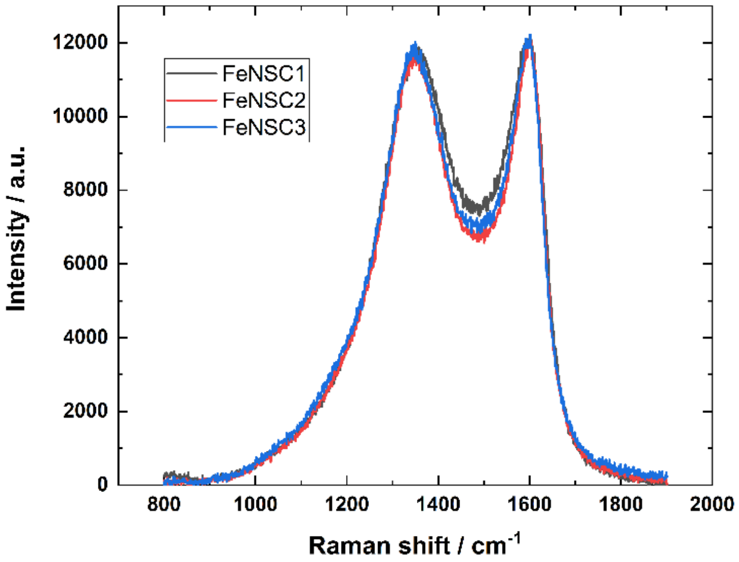

Fig. 5. Raman spectra of the FeNSC catalyst samples.

The I_{D1}/I_G ratios of FeNSC1, FeNSC2, and FeNSC3 catalysts are 3.7, 3.0, and 3.1 respectively. High value of this parameter indicates a significant presence of disorder and defects in the graphitic structure, meaning all prepared materials are quite amorphous, but among those FeNSC1 is slightly more disordered than FeNSC2 and FeNSC3. This can be explained by the preferential attack by NH_3 of the disordered carbon phase present initially in FeNSC1.

3.2 Oxygen reduction reaction studies on the FeNSC catalysts

The electroreduction of oxygen on FeNSC catalysts was investigated by the RRDE technique in O_2-saturated 0.1 M KOH electrolyte solution at 1600 rpm. In Fig. 6a, the RRDE polarisation curves of the prepared catalysts are compared with a commercial Pt/C catalyst. It can be seen that the electrochemical performance of FeNSC2 and FeNSC3 catalysts are similar. Although, FeNSC2 shows a slightly higher ORR performance than FeNSC3, half-wave potential ($E_{1/2}$) being 0.88 and 0.87 V, respectively. Interestingly, both catalysts slightly surpass the ORR activity of the Pt/C catalyst ($E_{1/2}$ = 0.84 V). The poorest ORR performance was observed for FeNSC1 catalyst ($E_{1/2}$ = 0.76 V). Higher electrocatalytic activity on FeNSC2 and FeNSC3 might be related to the materials synthesis, where NH_3 heat-treatment was employed while FeNSC1 was synthesized only via a single pyrolysis under N_2 flow. The addition of thiourea by ball-milling without subsequent pyrolysis may also have blocked some pores in FeNSC1, decreasing the O_2 and/ or electrolyte accessibility to some Fe-N_x active sites.

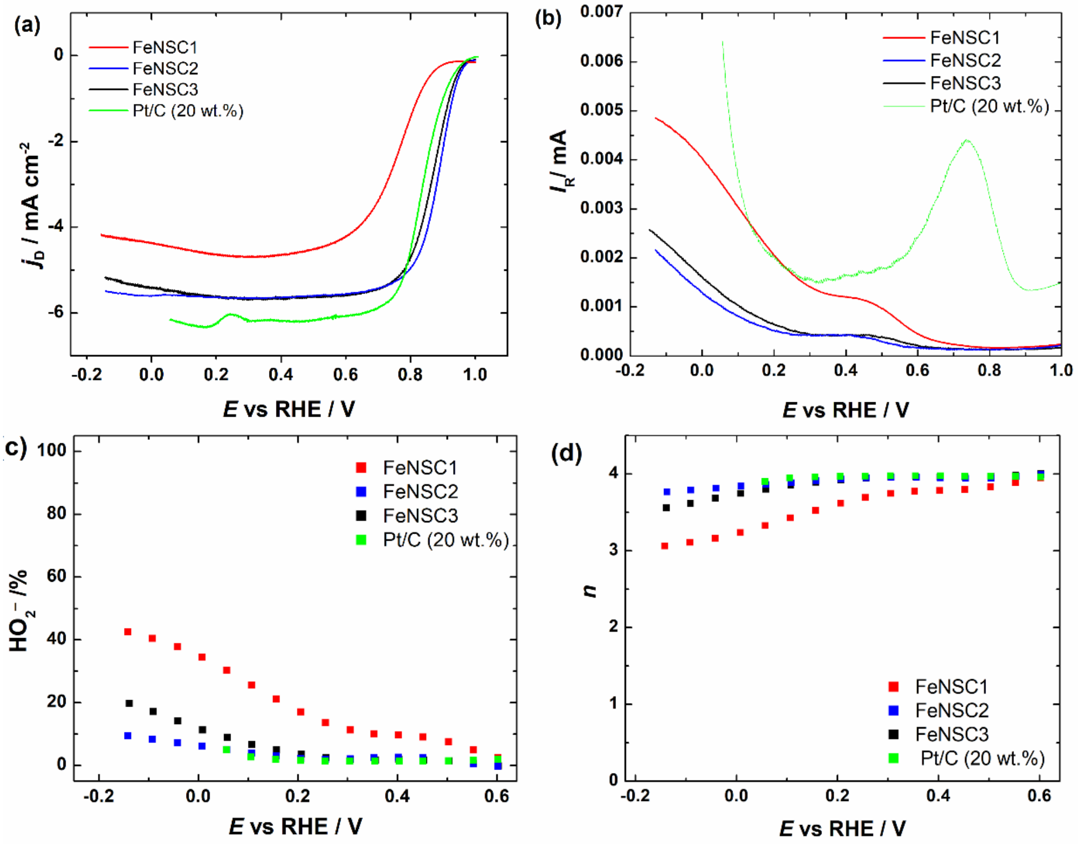

Fig 6. RRDE results for ORR on FeNSC and Pt/C (20 wt.%) catalysts: (a) disk current densities, (b) ring currents, (c) HO_2^- yield and (d) dependence of *n* on potential in O_2-saturated 0.1 M KOH solution at $\omega = 1600$ rpm and $\nu = 10$ mV s^{-1}. FeNSC catalyst loading: 0.2 mg cm^{-2}.

To collect more information on the ORR pathway, the data of the HO_2^- yield and the number of electrons transferred per O_2 molecule were obtained and the results are presented in Fig. 6c,d. The selectivity towards HO_2^- formation was quite low in a wide potential range for FeNSC2 and FeNSC3 electrocatalysts. The percentage of HO_2^- formation stayed close to zero in the case of FeNSC2 and FeNSC3 at high potentials ($E > 0.2$ V). At low potential ($E < 0.2$ V) the yield of HO_2^- increased to 10% and 20% for FeNSC2 and FeNSC3, respectively (see Fig. 6c). In the same potential range, FeNSC1 catalyst exhibited significantly higher yield of HO_2^-, up to 40% (Fig. 6c). The *n* value during the ORR process is close to four, only at more negative potentials the value decreased somewhat on FeNSC2 and FeNSC3 catalysts. This is in correlation with the percentage yield of HO_2^- formation. In the case of FeNSC1, the *n* value is between 3 and 4 (Fig. 6d). This indicates that the ORR process might occur via $2e^-$ and $4e^-$ pathway, where hydroperoxide anions are formed as intermediate and further reduced to OH^-.

The short-term stability of two best-performing catalyst materials was evaluated in 0.1 M KOH solution by measuring ORR polarisation curves at 1600 rpm before and after applying 10,000 potential cycles from 1 to 0.6 V at 200 mV s^{-1}. Both FeNSC2 and FeNSC3 catalysts displayed excellent stability (Fig. 7), as the polarisation curve remained virtually the same, the onset potentials did not change and only a minor shift of 4 mV in half-wave potential was observed with FeNSC3 material. Such impressive stability combined with good electrocatalytic activity shows potential applicability of these materials, especially FeNSC2 catalyst.

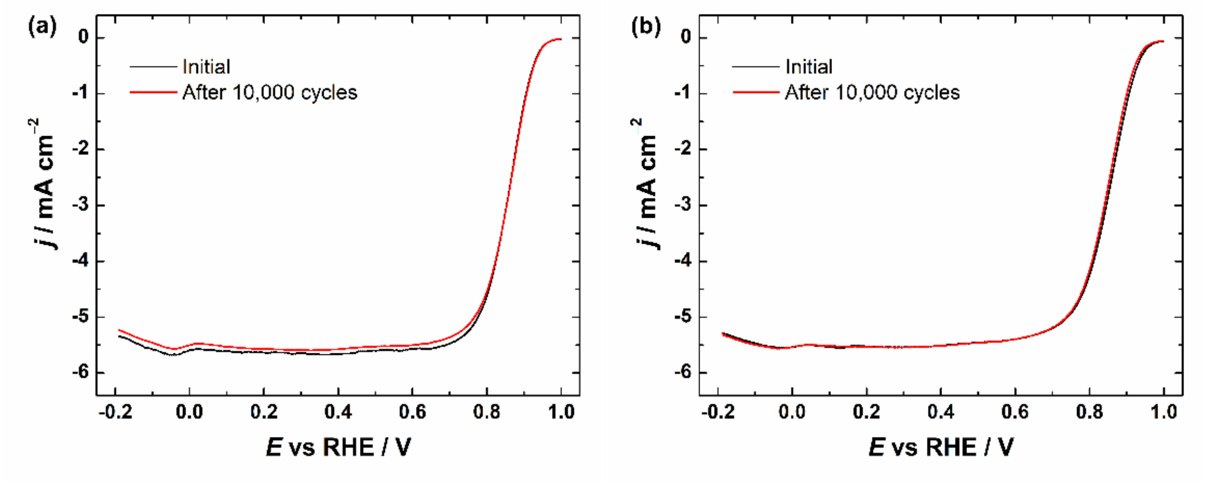

Figure 7. ORR polarisation curves of (a) FeNSC2 and (b) FeNSC3 catalyst in O_2-saturated 0.1 M KOH solution before and after 10,000 potential cycles (ω = 1600 rpm, ν = 10 mV s^{-1}).

The excellent electrocatalytic performance of FeNSC2 benefits from the following reasons. First, porous structure and high surface area of the catalyst. The higher SSA and microporous structure can lead to the formation of more ORR-active sites [11,20,80]. Second, the XPS analysis detected that, the most dominant nitrogen species in all the catalysts was pyridinic-N, which can increase the ORR onset potential of the catalyst [81]. Also, it has been proposed that pyridinic-N is one of the ORR-active sites and it is responsible for the reduction of HO_2^- to OH^- [81,82]. Other nitrogen moieties (confirmed by the XPS), like pyrrolic-N and graphitic-N are believed to improve the ORR performance as well [83,84]. Moreover, it is claimed that graphitic-N can increase the diffusion-limited current density and is responsible for the formation of HO_2^- [82]. Third, the presence of S in the catalyst. The synergetic effect between N and S can enhance electrocatalytic activity and favour a $4e^-$ pathway for the ORR [34,34,85]. Dual doping with heteroatoms also allows larger asymmetrical spin and higher charge density resulting larger number of active sites for the ORR to take place [34]. Finally, the presence of Fe-N_x active centres, especially in Fe-pyrrole-N_4 formation, on catalysts are known as highly active sites for ORR in alkaline and acidic media [86]. According to the literature, sulphur doping can lead to the structural change in carbon matrix and electronic structure by delocalising electrons from surrounding carbon atoms, thereby better interaction between Fe-N_x centres is achieved and the ORR activity of the catalyst is improved [81,87]. Different studies on Fe,N,S-doped carbon-based electrocatalysts can be found in the literature. For example, Li et al. synthesised Fe(Fc)-N/S-C catalyst, which exhibited a comparable electrocatalytic activity ($E_{1/2}$ = 0.87 V) to the catalysts prepared in this work [88]. They explained the improved activity with the formation of Fe-N or Fe-S sites. Tan et al. doped carbon nanotubes with Fe, N and S (Fe/N/S-PCNT) and achieved competitive ORR electrocatalytic performance with $E_{1/2}$ of 0.84 V, which is associated with the Fe–N–C and C–S–C active sites, high specific surface area and good hierarchical porous structure as the authors had pointed out [89]. The excellent ORR performance was confirmed by Jia et al. with half-wave potential on Fe-NSC catalyst of 0.92 V and the n value was calculated to be ~4 in the studied potential range [90]. The authors claimed that the great activity was influenced by the S doping-induced charge enrichment in N and Fe for optimal O_2 binding and fast electron transfer. Considering all this, we can assume that doping with heteroatoms (N and S) and iron is important to obtain an active catalyst for the ORR.

3.3 Anion-exchange membrane fuel cell test with FeNSC catalyst

Since the FeNSC2 showed the best ORR activity using the RRDE method, the catalyst was further tested as potential cathode catalyst in AEMFC configuration. Commercial Pt-Ru/C material was used for the anode and Aemion+ (AF2-HLE8-10-X, 10 µm) was applied as an AEM. Fig. 8 presents the AEMFC testing result. The FeNSC2 catalyst shows a moderate peak power density ($P_{\max}$) of 162 mW cm^{-2}, with the operating conditions and materials used.

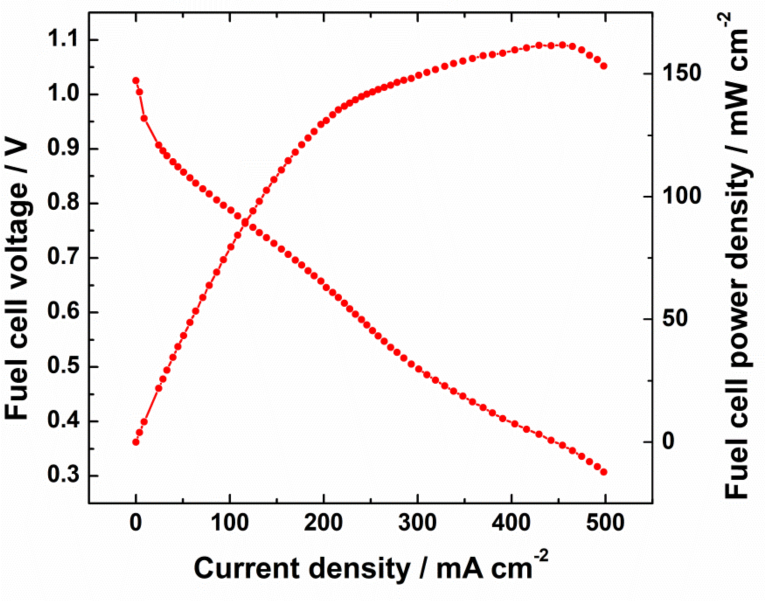

Fig. 8. Polarisation and power density curves for H_2/O_2 single-cell AEMFC using FeNSC2 as a cathode catalyst (2 mg cm^{-2}) along with Aemion+ (10 µm) AEM. Pt–Ru/C (0.8 mg$_{PtRu}$ cm^{-2}) was used as the anode catalyst. T = 65 °C. Flow rate for both O_2 and H_2 gases was 0.05 L min^{-1}.

No reports on the AEMFC performance of Fe, N and S triple-doped catalysts can be found. Therefore, it is difficult to compare the obtained results of AEMFC testing with the literature. Although there are numerous studies which have focused on catalysts co-doped with nitrogen and a transition metal, especially with an iron (Table 4). It can be seen that some catalysts have shown excellent performance compared to the results achieved in this work [91,92]. However, it should be noted that the used AEM is different. A similar AEMFC result (P_{max} = 220 mW cm^{-2}) was obtained by Lilloja et al. [25], who investigated iron and nitrogen-doped mesoporous carbon. The authors justified a lower P_{max} value with a thicker cathode catalyst layer and therefore, water management at high current densities might be more complicated [25]. In addition, the material's high microporosity and low mesoporosity may lead to poorer AEMFC performance. It is claimed that mesopores benefit in facilitating the transport of O_2 [11,16,80]. However, additional work needs to be done to optimise the operating conditions (temperature, humidity, pressure, flow rate of gases, backpressure, ionomer-to-catalyst ratio, water transport in the catalyst layer, etc.) to improve the AEM fuel cell performance.

Table 4. Comparison of H_2/O_2 AEMFC performances using iron-based cathode catalysts.

Cathode catalyst	Cathode loading (mg cm^{-2})	Anode loading (mg$_{PtRu}$ cm^{-2})	Membrane	T (˚C)	P_{max} (mW cm^{-2})	$j_{0.75\ V}$*, (mA cm^{-2})	Ref.
FeNCS2	2	0.8	Aemion+ (10 µm)	65	162	110	This work
Fe-N-Gra/CNT	1-1.25	0.72	Aemion+ (10 µm)	70	364	200	[93]
Fe/IL-PAN-A1000	2	0.6	HMT-PMBI	60	289	150	[94]
FeCoNC	2	0.6	HMT-PMBI	60	415	300	[95]
Fe-N-C	2	0.6	HMT-PMBI	60	220	260	[25]
Fe-N-Gra	2	0.6	HMT-PMBI	60	243	200	[36]
FeN-SiCDC-0.5-400-wet-PVP	2	0.8	HMT-PMBI	60	356	390	[96]
Fe-N-C-1000	4.5	0.5 Pt	FAA-3-50	60	149	100	[97]
Fe/pNC@HCF-1000	4	0.4 PtRu/C	FAA-3	60	343	100	[98]
Fe/N/CNT	2	0.4	aQAPS-S$_8$	60	490	150	[99]
Fe$_{0.5}$-NH$_3$	1.5	0.9	ETFE	60	1100	500	[91]
FeNx-CNTs	4	0.3	PVA-0.8PQVBC40%	60	1015	500	[92]

*Estimated from the Figures if value was not given at that potential

4. Conclusions

FeNSC catalysts for the ORR were synthesised using a simple ball-milling method, high-temperature pyrolysis and the two catalysts prepared were treated with NH_3. ZIF-8 was doped with iron, nitrogen and sulphur using iron(ii)acetate, 1,10-phenanthroline and thiourea as doping agents, respectively. The morphology of the catalysts was rather similar as revealed by SEM images. According to the N_2 physisorption analysis, all resulting catalysts exhibited high surface area, especially FeNSC2 and hierarchical porous structure (micro- and mesopores). Although, the prepared materials contained a greater amount of micropores. The XPS analysis detected very high nitrogen concentration in the catalysts, whereas the content of the other two elements (Fe, S) was relatively low in the resulting materials. Moreover, electrochemical studies carried out by the RRDE method displayed excellent ORR activity in alkaline media with a half-wave potential of 0.88 and 0.87 V for FeNSC2 and FeNSC3, respectively. In addition, the RRDE data showed low peroxide yield and the *n* value in the wide potential range was close to four for the FeNSC2 and FeNSC3 catalysts. In addition, these materials possessed excellent stability in alkaline media as the electrocatalytic activity almost did not change after 10,000 repetitive potential cycles. The AEMFC test conducted using FeNSC2 as a cathode catalyst exhibited moderate fuel cell performance with peak power density of 162 mW cm^{-2}.

Declaration of competing interest

The authors declare that they have no known competing financial interests or personal relationships that could have appeared to influence the work reported in this paper.

Data availability

Data will be made available on request.

Acknowledgements

This study was financially supported by the Estonian Research Council (grants PRG723, PRG4 and PRG1509) and EU through the European Regional Development Fund (TK141 “Advanced materials and high-technology devices for energy recuperation systems”, TK134 “Emerging orders in quantum and nanomaterials” and TK143 “Molecular Cell Engineering”). We thank Bernard Fraisse from ICGM for help with the XRD measurements.

References

[1] I. Staffell, D. Scamman, A.V. Abad, P. Balcombe, P.E. Dodds, P. Ekins, N. Shah, K.R. Ward, The role of hydrogen and fuel cells in the global energy system, Energy Environ. Sci. 12 (2019) 463–491. https://doi.org/10.1039/C8EE01157E.

[2] O. Gröger, H.A. Gasteiger, J.-P. Suchsland, Review—Electromobility: Batteries or Fuel Cells?, J. Electrochem. Soc. 162 (2015) A2605. https://doi.org/10.1149/2.0211514jes.

[3] N. Hassan, Catalytic performance of nanostructured materials recently used for developing fuel cells’ electrodes, Int. J. Hydrogen Energy 46 (2021) 39315–39368. https://doi.org/10.1016/j.ijhydene.2021.09.177.

[4] H. Nazir, N. Muthuswamy, C. Louis, S. Jose, J. Prakash, M.E.M. Buan, C. Flox, S. Chavan, X. Shi, P. Kauranen, T. Kallio, G. Maia, K. Tammeveski, N. Lymperopoulos, E. Carcadea, E. Veziroglu, A. Iranzo, A. M. Kannan, Is the H2 economy realizable in the

foreseeable future? Part III: H2 usage technologies, applications, and challenges and opportunities, Int. J. Hydrogen Energy 45 (2020) 28217–28239. https://doi.org/10.1016/j.ijhydene.2020.07.256.

[5] J. Hyun, H.-T. Kim, Powering the hydrogen future: current status and challenges of anion exchange membrane fuel cells, Energy Environ. Sci. 16 (2023) 5633–5662. https://doi.org/10.1039/D3EE01768K.

[6] N. Ramaswamy, S. Mukerjee, Alkaline Anion-Exchange Membrane Fuel Cells: Challenges in Electrocatalysis and Interfacial Charge Transfer, Chem. Rev. 119 (2019) 11945–11979. https://doi.org/10.1021/acs.chemrev.9b00157.

[7] M. Liu, X. Xiao, Q. Li, L. Luo, M. Ding, B. Zhang, Y. Li, J. Zou, B. Jiang, Recent progress of electrocatalysts for oxygen reduction in fuel cells, J. Colloid Interface Sci. 607 (2022) 791–815. https://doi.org/10.1016/j.jcis.2021.09.008.

[8] X. Zhang, H. Li, J. Yang, Y. Lei, C. Wang, J. Wang, Y. Tang, Z. Mao, Recent advances in Pt-based electrocatalysts for PEMFCs, RSC Adv. 11 (2021) 13316–13328. https://doi.org/10.1039/D0RA05468B.

[9] H. Li, H. Zhao, B. Tao, G. Xu, S. Gu, G. Wang, H. Chang, Pt-Based Oxygen Reduction Reaction Catalysts in Proton Exchange Membrane Fuel Cells: Controllable Preparation and Structural Design of Catalytic Layer, Nanomaterials 12 (2022) 4173. https://doi.org/10.3390/nano12234173.

[10] X. Ren, Q. Lv, L. Liu, B. Liu, Y. Wang, A. Liu, G. Wu, Current progress of Pt and Pt-based electrocatalysts used for fuel cells, Sustainable Energy Fuels 4 (2019) 15–30. https://doi.org/10.1039/C9SE00460B.

[11] A. Sarapuu, E. Kibena-Põldsepp, M. Borghei, K. Tammeveski, Electrocatalysis of oxygen reduction on heteroatom-doped nanocarbons and transition metal–nitrogen–carbon catalysts for alkaline membrane fuel cells, J. Mater. Chem. A 6 (2018) 776–804. https://doi.org/10.1039/C7TA08690C.

[12] Y. Nie, L. Li, Z. Wei, Recent advancements in Pt and Pt-free catalysts for oxygen reduction reaction, Chem. Soc. Rev. 44 (2015) 2168–2201. https://doi.org/10.1039/C4CS00484A.

[13] M. Shao, Q. Chang, J.-P. Dodelet, R. Chenitz, Recent Advances in Electrocatalysts for Oxygen Reduction Reaction, Chem. Rev. 116 (2016) 3594–3657. https://doi.org/10.1021/acs.chemrev.5b00462.

[14] A. Sarapuu, J. Lilloja, S. Akula, J.H. Zagal, S. Specchia, K. Tammeveski, Recent Advances in Non-Precious Metal Single-Atom Electrocatalysts for Oxygen Reduction Reaction in Low-Temperature Polymer-Electrolyte Fuel Cells, ChemCatChem 15 (2023) e202300849. https://doi.org/10.1002/cctc.202300849.

[15] J. Lilloja, E. Kibena-Põldsepp, A. Sarapuu, A. Kikas, V. Kisand, M. Käärik, M. Merisalu, A. Treshchalov, J. Leis, V. Sammelselg, Q. Wei, S. Holdcroft, K. Tammeveski, Nitrogen-doped carbide-derived carbon/carbon nanotube composites as cathode catalysts for anion exchange membrane fuel cell application, Appl. Catal. B: Environ. 272 (2020) 119012. https://doi.org/10.1016/j.apcatb.2020.119012.

[16] I. Palm, E. Kibena-Põldsepp, M. Mooste, J. Kozlova, M. Käärik, A. Kikas, A. Treshchalov, J. Leis, V. Kisand, A. Tamm, S. Holdcroft, P. Atanassov, K. Tammeveski, Nitrogen and Phosphorus Dual-Doped Silicon Carbide-Derived Carbon/Carbon Nanotube Composite for the Anion-Exchange Membrane Fuel Cell Cathode, ACS Appl. Energy Mater. 5 (2022) 2949-2958. https://doi.org/10.1021/acsaem.1c03627.

[17] R. Sibul, E. Kibena-Põldsepp, U. Mäeorg, M. Merisalu, A. Kikas, V. Kisand, A. Treshchalov, V. Sammelselg, K. Tammeveski, Sulphur and nitrogen co-doped graphene-based electrocatalysts for oxygen reduction reaction in alkaline medium, Electrochem. Commun. 109 (2019) 106603. https://doi.org/10.1016/j.elecom.2019.106603.

[18] R. Sibul, E. Kibena-Põldsepp, S. Ratso, M. Kook, M. Käärik, M. Merisalu, P. Paiste, J. Leis, V. Sammelselg, K. Tammeveski, Nitrogen-doped carbon-based electrocatalysts synthesised by ball-milling, Electrochem. Commun. 93 (2018) 39–43. https://doi.org/10.1016/j.elecom.2018.05.027.

[19] I. Palm, E. Kibena-Põldsepp, U. Mäeorg, J. Kozlova, M. Käärik, A. Kikas, J. Leis, V. Kisand, A. Tamm, K. Tammeveski, Silicon carbide-derived carbon electrocatalysts dual doped with nitrogen and phosphorus for the oxygen reduction reaction in an alkaline medium, Electrochem. Commun. 125 (2021) 106976. https://doi.org/10.1016/j.elecom.2021.106976.

[20] L. Yang, J. Shui, L. Du, Y. Shao, J. Liu, L. Dai, Z. Hu, Carbon-Based Metal-Free ORR Electrocatalysts for Fuel Cells: Past, Present, and Future, Adv. Mater. 31 (2019) 1804799. https://doi.org/10.1002/adma.201804799.

[21] K. Gao, B. Wang, L. Tao, B.V. Cunning, Z. Zhang, S. Wang, R.S. Ruoff, L. Qu, Efficient Metal-Free Electrocatalysts from N-Doped Carbon Nanomaterials: Mono-Doping and Co-Doping, Adv. Mater. 31 (2019) 1805121. https://doi.org/10.1002/adma.201805121.

[22] R. Praats, M. Käärik, A. Kikas, V. Kisand, J. Aruväli, P. Paiste, M. Merisalu, J. Leis, V. Sammelselg, J.H. Zagal, S. Holdcroft, N. Nakashima, K. Tammeveski, Electrocatalytic oxygen reduction reaction on iron phthalocyanine-modified carbide-derived carbon/carbon nanotube composite electrocatalysts, Electrochim. Acta 334 (2020) 135575. https://doi.org/10.1016/j.electacta.2019.135575.

[23] S. Ratso, N.R. Sahraie, M.T. Sougrati, M. Käärik, M. Kook, R. Saar, P. Paiste, Q. Jia, J. Leis, S. Mukerjee, F. Jaouen, K. Tammeveski, Synthesis of highly-active Fe–N–C catalysts for PEMFC with carbide-derived carbons, J. Mater. Chem. A 6 (2018) 14663–14674. https://doi.org/10.1039/C8TA02325E.

[24] J. Lilloja, E. Kibena-Põldsepp, A. Sarapuu, J.C. Douglin, M. Käärik, J. Kozlova, P. Paiste, A. Kikas, J. Aruväli, J. Leis, V. Sammelselg, D.R. Dekel, K. Tammeveski, Transition-Metal- and Nitrogen-Doped Carbide-Derived Carbon/Carbon Nanotube Composites as Cathode Catalysts for Anion-Exchange Membrane Fuel Cells, ACS Catal. 11 (2021) 1920–1931. https://doi.org/10.1021/acscatal.0c03511.

[25] J. Lilloja, M. Mooste, E. Kibena-Põldsepp, A. Sarapuu, B. Zulevi, A. Kikas, H.-M. Piirsoo, A. Tamm, V. Kisand, S. Holdcroft, A. Serov, K. Tammeveski, Mesoporous iron-nitrogen co-doped carbon material as cathode catalyst for the anion exchange membrane fuel cell, J. Power Sources Adv. 8 (2021) 100052. https://doi.org/10.1016/j.powera.2021.100052.

[26] A. Zitolo, N. Ranjbar-Sahraie, T. Mineva, J. Li, Q. Jia, S. Stamatin, G.F. Harrington, S.M. Lyth, P. Krtil, S. Mukerjee, E. Fonda, F. Jaouen, Identification of catalytic sites in cobalt-nitrogen-carbon materials for the oxygen reduction reaction, Nat. Commun. 8 (2017) 957. https://doi.org/10.1038/s41467-017-01100-7.

[27] K. Kisand, A. Sarapuu, J.C. Douglin, A. Kikas, A. Treshchalov, M. Käärik, H.-M. Piirsoo, P. Paiste, J. Aruväli, J. Leis, V. Kisand, A. Tamm, D.R. Dekel, K. Tammeveski, Templated Nitrogen-, Iron-, and Cobalt-Doped Mesoporous Nanocarbon Derived from an Alkylresorcinol Mixture for Anion-Exchange Membrane Fuel Cell Application, ACS Catal. 12 (2022) 14050–14061. https://doi.org/10.1021/acscatal.2c03683.

[28] K. Muuli, A. Sokka, M. Mooste, J. Lilloja, V. Gudkova, M. Käärik, M. Otsus, A. Kikas, V. Kisand, A. Tamm, J. Leis, A. Krumme, S. Holdcroft, J.H. Zagal, K. Tammeveski, Iron and cobalt phthalocyanine embedded electrospun carbon nanofiber-based catalysts for anion exchange membrane fuel cell cathode, J. Catal. 422 (2023) 117–130. https://doi.org/10.1016/j.jcat.2023.04.008.

[29] S. Juvanen, A. Sarapuu, M. Mooste, M. Käärik, U. Mäeorg, A. Kikas, V. Kisand, J. Kozlova, A. Treshchalov, J. Aruväli, J. Leis, A. Tamm, K. Tammeveski, Electroreduction of oxygen on iron- and cobalt-containing nitrogen-doped carbon catalysts prepared from the rapeseed press cake, J. Electroanal. Chem. 920 (2022) 116599. https://doi.org/10.1016/j.jelechem.2022.116599.

[30] K. Gong, F. Du, Z. Xia, M. Durstock, L. Dai, Nitrogen-Doped Carbon Nanotube Arrays with High Electrocatalytic Activity for Oxygen Reduction, Science 323 (2009) 760–764. https://doi.org/10.1126/science.1168049.

[31] M. Vikkisk, I. Kruusenberg, U. Joost, E. Shulga, I. Kink, K. Tammeveski, Electrocatalytic oxygen reduction on nitrogen-doped graphene in alkaline media, Appl. Catal. B: Environ. 147 (2014) 369–376. https://doi.org/10.1016/j.apcatb.2013.09.011.

[32] Z. Wu, R. Liu, J. Wang, J. Zhu, W. Xiao, C. Xuan, W. Lei, D. Wang, Nitrogen and sulfur co-doping of 3D hollow-structured carbon spheres as an efficient and stable metal free catalyst for the oxygen reduction reaction, Nanoscale 8 (2016) 19086–19092. https://doi.org/10.1039/C6NR06817K.

[33] K. Preuss, A.M. Siwoniku, C.I. Bucur, M.-M. Titirici, The Influence of Heteroatom Dopants Nitrogen, Boron, Sulfur, and Phosphorus on Carbon Electrocatalysts for the Oxygen Reduction Reaction, ChemPlusChem 84 (2019) 457–464. https://doi.org/10.1002/cplu.201900083.

[34] S. Bag, B. Mondal, A.K. Das, C.R. Raj, Nitrogen and Sulfur Dual-Doped Reduced Graphene Oxide: Synergistic Effect of Dopants Towards Oxygen Reduction Reaction, Electrochim. Acta 163 (2015) 16–23. https://doi.org/10.1016/j.electacta.2015.02.130.

[35] S. Ratso, M. Käärik, M. Kook, P. Paiste, J. Aruväli, S. Vlassov, V. Kisand, J. Leis, A.M. Kannan, K. Tammeveski, High performance catalysts based on Fe/N co-doped carbide-derived carbon and carbon nanotube composites for oxygen reduction reaction in acid media, Int. J. Hydrogen Energy 44 (2019) 12636–12648. https://doi.org/10.1016/j.ijhydene.2018.11.080.

[36] R. Sibul, E. Kibena-Põldsepp, S. Ratso, M. Kook, M.T. Sougrati, M. Käärik, M. Merisalu, J. Aruväli, P. Paiste, A. Treshchalov, J. Leis, V. Kisand, V. Sammelselg, S. Holdcroft, F. Jaouen, K. Tammeveski, Iron- and Nitrogen-Doped Graphene-Based Catalysts for Fuel Cell Applications, ChemElectroChem 7 (2020) 1739–1747. https://doi.org/10.1002/celc.202000011.

[37] Y. Mun, M.J. Kim, S.-A. Park, E. Lee, Y. Ye, S. Lee, Y.-T. Kim, S. Kim, O.-H. Kim, Y.-H. Cho, Y.-E. Sung, J. Lee, Soft-template synthesis of mesoporous non-precious metal catalyst with Fe-Nx/C active sites for oxygen reduction reaction in fuel cells, Appl. Catal. B: Environ. 222 (2018) 191–199. https://doi.org/10.1016/j.apcatb.2017.10.015.

[38] M.M. Hossen, K. Artyushkova, P. Atanassov, A. Serov, Synthesis and characterization of high performing Fe-N-C catalyst for oxygen reduction reaction (ORR) in Alkaline Exchange Membrane Fuel Cells, J. Power Sources 375 (2018) 214–221. https://doi.org/10.1016/j.jpowsour.2017.08.036.

[39] J. Lilloja, M. Mooste, E. Kibena-Põldsepp, A. Sarapuu, A. Kikas, V. Kisand, M. Käärik, J. Kozlova, A. Treshchalov, P. Paiste, J. Aruväli, J. Leis, A. Tamm, S. Holdcroft, K. Tammeveski, Cobalt-, iron- and nitrogen-containing ordered mesoporous carbon-based catalysts for anion-exchange membrane fuel cell cathode, Electrochim. Acta 439 (2023) 141676. https://doi.org/10.1016/j.electacta.2022.141676.

[40] J. Lilloja, E. Kibena-Põldsepp, A. Sarapuu, M. Käärik, J. Kozlova, P. Paiste, A. Kikas, A. Treshchalov, J. Leis, A. Tamm, V. Kisand, S. Holdcroft, K. Tammeveski, Transition metal and nitrogen-doped mesoporous carbons as cathode catalysts for anion-exchange membrane fuel cells, Appl. Catal. B: Environ. 306 (2022) 121113. https://doi.org/10.1016/j.apcatb.2022.121113.

[41] Y. Kumar, E. Kibena-Põldsepp, M. Mooste, J. Kozlova, A. Kikas, J. Aruväli, M. Käärik, V. Kisand, J. Leis, A. Tamm, S. Holdcroft, J.H. Zagal, K. Tammeveski, Iron and Nickel Phthalocyanine-Modified Nanocarbon Materials as Cathode Catalysts for Anion-Exchange Membrane Fuel Cells and Zinc-Air Batteries, ChemElectroChem 9 (2022) e202200717. https://doi.org/10.1002/celc.202200717.

[42] S. Akula, M. Mooste, J. Kozlova, M. Käärik, A. Treshchalov, A. Kikas, V. Kisand, J. Aruväli, P. Paiste, A. Tamm, J. Leis, K. Tammeveski, Transition metal (Fe, Co, Mn, Cu) containing nitrogen-doped porous carbon as efficient oxygen reduction electrocatalysts for anion exchange membrane fuel cells, Chem. Eng. J. 458 (2023) 141468. https://doi.org/10.1016/j.cej.2023.141468.

[43] Md.M. Hossen, Md.S. Hasan, Md.R.I. Sardar, J. bin Haider, Mottakin, K. Tammeveski, P. Atanassov, State-of-the-art and developmental trends in platinum group metal-free cathode catalyst for anion exchange membrane fuel cell (AEMFC), Appl. Catal. B: Environ. 325 (2023) 121733. https://doi.org/10.1016/j.apcatb.2022.121733.

[44] Q. Jia, N. Ramaswamy, U. Tylus, K. Strickland, J. Li, A. Serov, K. Artyushkova, P. Atanassov, J. Anibal, C. Gumeci, S.C. Barton, M.-T. Sougrati, F. Jaouen, B. Halevi, S. Mukerjee, Spectroscopic insights into the nature of active sites in iron–nitrogen–carbon electrocatalysts for oxygen reduction in acid, Nano Energy 29 (2016) 65–82. https://doi.org/10.1016/j.nanoen.2016.03.025.

[45] A. Zitolo, V. Goellner, V. Armel, M.-T. Sougrati, T. Mineva, L. Stievano, E. Fonda, F. Jaouen, Identification of catalytic sites for oxygen reduction in iron- and nitrogen-doped graphene materials, Nat. Mater. 14 (2015) 937–942. https://doi.org/10.1038/nmat4367.

[46] S. Ratso, M.T. Sougrati, M. Käärik, M. Merisalu, M. Rähn, V. Kisand, A. Kikas, P. Paiste, J. Leis, V. Sammelselg, F. Jaouen, K. Tammeveski, Effect of Ball-Milling on the Oxygen Reduction Reaction Activity of Iron and Nitrogen Co-doped Carbide-Derived Carbon Catalysts in Acid Media, ACS Appl. Energy Mater. 2 (2019) 7952–7962. https://doi.org/10.1021/acsaem.9b01430.

[47] Z. Ahmed, S. Akula, J. Kozlova, H.-M. Piirsoo, K. Kukli, A. Kikas, V. Kisand, M. Käärik, J. Leis, A. Treshchalov, J. Aruväli, K. Tammeveski, Hybrid high-performance oxygen reduction reaction Fe–N–C electrocatalyst for anion exchange membrane fuel cells, Int. J. Hydrogen Energy 62 (2024) 849–858. https://doi.org/10.1016/j.ijhydene.2024.03.055.

[48] K. Ping, A. Braschinsky, M. Alam, R. Bhadoria, V. Mikli, A. Mere, J. Aruväli, P. Paiste, S. Vlassov, M. Kook, M. Rähn, V. Sammelselg, K. Tammeveski, N. Kongi, P. Starkov, Fused Hybrid Linkers for Metal–Organic Framework-Derived Bifunctional Oxygen Electrocatalysts, ACS Appl. Energy Mater. 3 (2020) 152–157. https://doi.org/10.1021/acsaem.9b02039.

[49] S.S.A. Shah, T. Najam, M.K. Aslam, M. Ashfaq, M.M. Rahman, K. Wang, P. Tsiakaras, S. Song, Y. Wang, Recent advances on oxygen reduction electrocatalysis: Correlating the characteristic properties of metal organic frameworks and the derived nanomaterials, Appl. Catal. B: Environ. 268 (2020) 118570. https://doi.org/10.1016/j.apcatb.2019.118570.

[50] L. Zhang, Z. Su, F. Jiang, L. Yang, J. Qian, Y. Zhou, W. Li, M. Hong, Highly graphitized nitrogen-doped porous carbon nanopolyhedra derived from ZIF-8 nanocrystals as efficient electrocatalysts for oxygen reduction reactions, Nanoscale 6 (2014) 6590–6602. https://doi.org/10.1039/C4NR00348A.

[51] A. Mahmood, W. Guo, H. Tabassum, R. Zou, Metal-Organic Framework-Based Nanomaterials for Electrocatalysis, Adv. Energy Mater. 6 (2016) 1600423. https://doi.org/10.1002/aenm.201600423.

[52] L. Yang, X. Zeng, W. Wang, D. Cao, Recent Progress in MOF-Derived, Heteroatom-Doped Porous Carbons as Highly Efficient Electrocatalysts for Oxygen Reduction Reaction in Fuel Cells, Adv. Funct. Mater. 28 (2018) 1704537. https://doi.org/10.1002/adfm.201704537.

[53] J. Li, Y. Chen, Y. Tang, S. Li, H. Dong, K. Li, M. Han, Y.-Q. Lan, J. Bao, Z. Dai, Metal–organic framework templated nitrogen and sulfur co-doped porous carbons as highly efficient metal-free electrocatalysts for oxygen reduction reactions, J. Mater. Chem. A 2 (2014) 6316–6319. https://doi.org/10.1039/C3TA15335E.

[54] A. Morozan, F. Jaouen, Metal organic frameworks for electrochemical applications, Energy Environ. Sci. 5 (2012) 9269–9290. https://doi.org/10.1039/C2EE22989G.

[55] Y. Xu, Q. Li, H. Xue, H. Pang, Metal-organic frameworks for direct electrochemical applications, Coord. Chem. Rev. 376 (2018) 292–318. https://doi.org/10.1016/j.ccr.2018.08.010.

[56] J.-K. Sun, Q. Xu, Functional materials derived from open framework templates/precursors: synthesis and applications, Energy Environ. Sci. 7 (2014) 2071–2100. https://doi.org/10.1039/C4EE00517A.

[57] G. Xu, P. Nie, H. Dou, B. Ding, L. Li, X. Zhang, Exploring metal organic frameworks for energy storage in batteries and supercapacitors, Mater. Today 20 (2017) 191–209. https://doi.org/10.1016/j.mattod.2016.10.003.

[58] K.S. Park, Z. Ni, A.P. Côté, J.Y. Choi, R. Huang, F.J. Uribe-Romo, H.K. Chae, M. O’Keeffe, O.M. Yaghi, Exceptional chemical and thermal stability of zeolitic imidazolate frameworks, Proc. Nat. Acad. Sci. U.S.A. 103 (2006) 10186–10191. https://doi.org/10.1073/pnas.0602439103.

[59] H. Wu, W. Zhou, T. Yildirim, Hydrogen Storage in a Prototypical Zeolitic Imidazolate Framework-8, J. Am. Chem. Soc. 129 (2007) 5314–5315. https://doi.org/10.1021/ja0691932.

[60] H. Zhong, J. Wang, Y. Zhang, W. Xu, W. Xing, D. Xu, Y. Zhang, X. Zhang, ZIF-8 Derived Graphene-Based Nitrogen-Doped Porous Carbon Sheets as Highly Efficient and Durable Oxygen Reduction Electrocatalysts, Angew. Chem. Int. Ed. 53 (2014) 14235–14239. https://doi.org/10.1002/anie.201408990.

[61] Y.-Z. Chen, C. Wang, Z.-Y. Wu, Y. Xiong, Q. Xu, S.-H. Yu, H.-L. Jiang, From Bimetallic Metal-Organic Framework to Porous Carbon: High Surface Area and Multicomponent Active Dopants for Excellent Electrocatalysis, Adv. Mater. 27 (2015) 5010–5016. https://doi.org/10.1002/adma.201502315.

[62] E. Proietti, F. Jaouen, M. Lefèvre, N. Larouche, J. Tian, J. Herranz, J.-P. Dodelet, Iron-based cathode catalyst with enhanced power density in polymer electrolyte membrane fuel cells, Nat. Commun. 2 (2011) 416. https://doi.org/10.1038/ncomms1427.

[63] P.G. Santori, F.D. Speck, J. Li, A. Zitolo, Q. Jia, S. Mukerjee, S. Cherevko, F. Jaouen, Effect of Pyrolysis Atmosphere and Electrolyte pH on the Oxygen Reduction Activity, Stability and Spectroscopic Signature of FeNx Moieties in Fe-N-C Catalysts, J. Electrochem. Soc. 166 (2019) F3311. https://doi.org/10.1149/2.0371907jes.

[64] D.R. Dekel, Review of cell performance in anion exchange membrane fuel cells, J. Power Sources 375 (2018) 158–169. https://doi.org/10.1016/j.jpowsour.2017.07.117.

[65] R. Sgarbi, K. Kumar, F. Jaouen, A. Zitolo, E.A. Ticianelli, F. Maillard, Oxygen reduction reaction mechanism and kinetics on M-NxCy and M@N-C active sites present in model M-N-C catalysts under alkaline and acidic conditions, J. Solid State Electrochem. 25 (2021) 45–56. https://doi.org/10.1007/s10008-019-04436-w.

[66] A.G. Wright, J. Fan, B. Britton, T. Weissbach, H.-F. Lee, E.A. Kitching, T.J. Peckham, S. Holdcroft, Hexamethyl-p-terphenyl poly(benzimidazolium): a universal

hydroxide-conducting polymer for energy conversion devices, Energy Environ. Sci. 9 (2016) 2130–2142. https://doi.org/10.1039/C6EE00656F.

[67] M. Thommes, K. Kaneko, A.V. Neimark, J.P. Olivier, F. Rodriguez-Reinoso, J. Rouquerol, K.S.W. Sing, Physisorption of gases, with special reference to the evaluation of surface area and pore size distribution (IUPAC Technical Report), Pure Appl. Chem. 87 (2015) 1051–1069. https://doi.org/10.1515/pac-2014-1117.

[68] T.-N. Tran, C.-H. Shin, B.-J. Lee, J.S. Samdani, J.-D. Park, T.-H. Kang, J.-S. Yu, Fe–N-functionalized carbon electrocatalyst derived from a zeolitic imidazolate framework for oxygen reduction: Fe and NH3 treatment effects, Catal. Sci. Technol. 8 (2018) 5368–5381. https://doi.org/10.1039/C8CY01140K.

[69] F. Jaouen, A.M. Serventi, M. Lefèvre, J.-P. Dodelet, P. Bertrand, Non-Noble Electrocatalysts for O2 Reduction: How Does Heat Treatment Affect Their Activity and Structure? Part II. Structural Changes Observed by Electron Microscopy, Raman, and Mass Spectroscopy, J. Phys. Chem. C 111 (2007) 5971-5976. https://doi.org/10.1021/jp068274h.

[70] F. Jaouen, J.-P. Dodelet, Non-Noble Electrocatalysts for O2 Reduction: How Does Heat Treatment Affect Their Activity and Structure? Part I. Model for Carbon Black Gasification by NH3: Parametric Calibration and Electrochemical Validation, J. Phys. Chem. C 111 (2007) 5963–5970. https://doi.org/10.1021/jp068273p.

[71] S. Fu, C. Zhu, J. Song, M.H. Engelhard, X. Li, P. Zhang, H. Xia, D. Du, Y. Lin, Template-directed synthesis of nitrogen- and sulfur-codoped carbon nanowire aerogels with enhanced electrocatalytic performance for oxygen reduction, Nano Res. 10 (2017) 1888–1895. https://doi.org/10.1007/s12274-016-1371-8.

[72] H. Zhao, Y.-P. Zhu, L. Ge, Z.-Y. Yuan, Nitrogen and sulfur co-doped mesoporous hollow carbon microspheres for highly efficient oxygen reduction electrocatalysts, Int. J. Hydrogen Energy 42 (2017) 19010–19018. https://doi.org/10.1016/j.ijhydene.2017.06.172.

[73] Y. Li, J. Yang, J. Huang, Y. Zhou, K. Xu, N. Zhao, X. Cheng, Soft template-assisted method for synthesis of nitrogen and sulfur co-doped three-dimensional reduced graphene oxide as an efficient metal free catalyst for oxygen reduction reaction, Carbon 122 (2017) 237–246. https://doi.org/10.1016/j.carbon.2017.06.046.

[74] Y. Lv, L. Yang, D. Cao, Sulfur, Nitrogen and Fluorine Triple-Doped Metal-Free Carbon Electrocatalysts for the Oxygen Reduction Reaction, ChemElectroChem 6 (2019) 741–747. https://doi.org/10.1002/celc.201801433.

[75] Z. Liu, H. Nie, Z. Yang, J. Zhang, Z. Jin, Y. Lu, Z. Xiao, S. Huang, Sulfur–nitrogen co-doped three-dimensional carbon foams with hierarchical pore structures as efficient metal-free electrocatalysts for oxygen reduction reactions, Nanoscale 5 (2013) 3283–3288. https://doi.org/10.1039/C3NR34003A.

[76] H. Yu, J. Hou, R.B. Namin, Y. Ni, S. Liu, S. Yu, Y. Liu, Q. Wu, S. Nie, Pre-cryocrushing of natural carbon precursors to prepare nitrogen, sulfur co-doped porous microcellular carbon as an efficient ORR catalyst, Carbon 173 (2021) 800–808. https://doi.org/10.1016/j.carbon.2020.11.069.

[77] M.J. Dzara, K. Artyushkova, M.T. Sougrati, C. Ngo, M.A. Fitzgerald, A. Serov, B. Zulevi, P. Atanassov, F. Jaouen, S. Pylypenko, Characterizing Complex Gas–Solid Interfaces with in Situ Spectroscopy: Oxygen Adsorption Behavior on Fe–N–C Catalysts, J. Phys. Chem. C 124 (2020) 16529–16543. https://doi.org/10.1021/acs.jpcc.0c05244.

[78] M.V. Glazoff, A. Tokuhiro, S.N. Rashkeev, P. Sabharwall, Oxidation and hydrogen uptake in zirconium, Zircaloy-2 and Zircaloy-4: Computational thermodynamics and ab initio calculations, J. Nuclear Mater. 444 (2014) 65–75. https://doi.org/10.1016/j.jnucmat.2013.09.038.

[79] A. Sadezky, H. Muckenhuber, H. Grothe, R. Niessner, U. Pöschl, Raman microspectroscopy of soot and related carbonaceous materials: Spectral analysis and structural information, Carbon 43 (2005) 1731–1742. https://doi.org/10.1016/j.carbon.2005.02.018.

[80] A. Gabe, R. Ruiz-Rosas, C. González-Gaitán, E. Morallón, D. Cazorla-Amorós, Modeling of oxygen reduction reaction in porous carbon materials in alkaline medium. Effect of microporosity, J. Power Sources 412 (2019) 451–464. https://doi.org/10.1016/j.jpowsour.2018.11.075.

[81] S. Guo, J. Hu, S. Luo, Y. Zhang, Z. Zhang, P. Dong, X. Zeng, M. Xu, L. Han, J. Yuan, C. Zhang, Y. Zhang, Zr enhanced Fe, N, S co-doped carbon-based catalyst for high-efficiency oxygen reduction reaction, Int. J. Hydrogen Energy 47 (2022) 8348–8358. https://doi.org/10.1016/j.ijhydene.2021.12.209.

[82] S. Kabir, K. Artyushkova, A. Serov, P. Atanassov, Role of Nitrogen Moieties in N-Doped 3D-Graphene Nanosheets for Oxygen Electroreduction in Acidic and Alkaline Media, ACS Appl. Mater. Interfaces 10 (2018) 11623–11632. https://doi.org/10.1021/acsami.7b18651.

[83] M. Mooste, E. Kibena-Põldsepp, V. Vassiljeva, M. Merisalu, M. Kook, A. Treshchalov, V. Kisand, M. Uibu, A. Krumme, V. Sammelselg, K. Tammeveski, Electrocatalysts for oxygen reduction reaction based on electrospun polyacrylonitrile, styrene–acrylonitrile copolymer and carbon nanotube composite fibres, J Mater Sci 54 (2019) 11618–11634. https://doi.org/10.1007/s10853-019-03725-z.

[84] S.M. Unni, S. Devulapally, N. Karjule, S. Kurungot, Graphene enriched with pyrrolic coordination of the doped nitrogen as an efficient metal-free electrocatalyst for oxygen reduction, J. Mater. Chem. 22 (2012) 23506–23513. https://doi.org/10.1039/C2JM35547G.

[85] T. Oh, K. Kim, J. Kim, Controllable active sites and facile synthesis of cobalt nanoparticle embedded in nitrogen and sulfur co-doped carbon nanotubes as efficient bifunctional electrocatalysts for oxygen reduction and evolution reactions, J. Energy Chem. 38 (2019) 60–67. https://doi.org/10.1016/j.jechem.2018.12.021.

[86] D. Zhang, Z. Wang, F. Liu, P. Yi, L. Peng, Y. Chen, L. Wei, H. Li, Unraveling the pH-Dependent Oxygen Reduction Performance on Single-Atom Catalysts: From Single- to Dual-Sabatier Optima, J. Am. Chem. Soc. 146 (2024) 3210–3219. https://doi.org/10.1021/jacs.3c11246.

[87] X. Qu, Y. Li, G. Li, R. Ji, S. Yin, X. Cheng, C. Wang, J. Yang, Y. Jiang, S. Sun, Boosting the ORR performance of Fe-N/C catalyst via increasing the density and modifying the electronic structure of Fe-NX active sites, Electrochim. Acta 403 (2022) 139604. https://doi.org/10.1016/j.electacta.2021.139604.

[88] X. Li, X. Yang, L. Liu, H. Zhao, Y. Li, H. Zhu, Y. Chen, S. Guo, Y. Liu, Q. Tan, G. Wu, Chemical Vapor Deposition for N/S-Doped Single Fe Site Catalysts for the Oxygen Reduction in Direct Methanol Fuel Cells, ACS Catal. 11 (2021) 7450–7459. https://doi.org/10.1021/acscatal.0c05446.

[89] Z. Tan, H. Li, Q. Feng, L. Jiang, H. Pan, Z. Huang, Q. Zhou, H. Zhou, S. Ma, Y. Kuang, One-pot synthesis of Fe/N/S-doped porous carbon nanotubes for efficient oxygen reduction reaction, J. Mater. Chem. A 7 (2019) 1607–1615. https://doi.org/10.1039/C8TA09589B.

[90] Y. Jia, X. Xiong, D. Wang, X. Duan, K. Sun, Y. Li, L. Zheng, W. Lin, M. Dong, G. Zhang, W. Liu, X. Sun, Atomically Dispersed Fe-N4 Modified with Precisely Located S for Highly Efficient Oxygen Reduction, Nano-Micro Lett. 12 (2020) 116. https://doi.org/10.1007/s40820-020-00456-8.

[91] P.G. Santori, F.D. Speck, S. Cherevko, H.A. Firouzjaie, X. Peng, W.E. Mustain, F. Jaouen, High Performance FeNC and Mn-oxide/FeNC Layers for AEMFC Cathodes, J. Electrochem. Soc. 167 (2020) 134505. https://doi.org/10.1149/1945-7111/abb7e0.

[92] Q. He, L. Zeng, J. Wang, J. Jiang, L. Zhang, J. Wang, W. Ding, Z. Wei, Polymer-coating-induced synthesis of FeNx enriched carbon nanotubes as cathode that exceeds 1.0 W cm−2 peak power in both proton and anion exchange membrane fuel cells, J. Power Sources 489 (2021) 229499. https://doi.org/10.1016/j.jpowsour.2021.229499.

[93] J. Lilloja, E. Kibena-Põldsepp, A. Sarapuu, A. Konovalova, M. Käärik, J. Kozlova, P. Paiste, A. Kikas, A. Treshchalov, J. Aruväli, A. Zitolo, J. Leis, A. Tamm, V. Kisand, S. Holdcroft, K. Tammeveski, Transition-Metal and Nitrogen-Doped Carbon Nanotube/Graphene Composites as Cathode Catalysts for Anion-Exchange Membrane Fuel Cells, ACS Appl. Energy Mater. 6 (2023) 5519-5529. https://doi.org/10.1021/acsaem.3c00613.

[94] M. Mooste, E. Kibena-Põldsepp, V. Vassiljeva, A. Kikas, M. Käärik, J. Kozlova, V. Kisand, M. Külaviir, S. Cavaliere, J. Leis, A. Krumme, V. Sammelselg, S. Holdcroft, K. Tammeveski, Electrospun Polyacrylonitrile-Derived Co or Fe Containing Nanofibre Catalysts for Oxygen Reduction Reaction at the Alkaline Membrane Fuel Cell Cathode, ChemCatChem 12 (2020) 4568–4581. https://doi.org/10.1002/cctc.202000658.

[95] K. Kisand, A. Sarapuu, D. Danilian, A. Kikas, V. Kisand, M. Rähn, A. Treshchalov, M. Käärik, M. Merisalu, P. Paiste, J. Aruväli, J. Leis, V. Sammelselg, S. Holdcroft, K. Tammeveski, Transition metal-containing nitrogen-doped nanocarbon catalysts derived from 5-methylresorcinol for anion exchange membrane fuel cell application, J. Colloid Interface Sci. 584 (2021) 263–274. https://doi.org/10.1016/j.jcis.2020.09.114.

[96] S. Ratso, A. Zitolo, M. Käärik, M. Merisalu, A. Kikas, V. Kisand, M. Rähn, P. Paiste, J. Leis, V. Sammelselg, S. Holdcroft, F. Jaouen, K. Tammeveski, Non-precious metal cathodes for anion exchange membrane fuel cells from ball-milled iron and nitrogen doped carbide-derived carbons, Renewable Energy 167 (2021) 800–810. https://doi.org/10.1016/j.renene.2020.11.154.

[97] W. Freitas, A. D’Epifanio, C. Vecchio, I. Gatto, V. Baglio, V.C.A. Ficca, E. Placidi, B. Mecheri, Tailoring MOF Structure via Iron Decoration to Enhance ORR in Alkaline Polymer Electrolyte Membrane Fuel Cells, Chem. Eng. J. 465 (2023) 142987. https://doi.org/10.1016/j.cej.2023.142987.

[98] G.-S. Kang, J.-H. Jang, S.-Y. Son, Y.-K. Lee, D.C. Lee, S.J. Yoo, S. Lee, H.-I. Joh, Pyrrolic N wrapping strategy to maximize the number of single-atomic Fe-Nx sites for oxygen reduction reaction, J. Power Sources 520 (2022) 230904. https://doi.org/10.1016/j.jpowsour.2021.230904.

[99] H. Ren, Y. Wang, Y. Yang, X. Tang, Y. Peng, H. Peng, L. Xiao, J. Lu, H.D. Abruña, L. Zhuang, Fe/N/C Nanotubes with Atomic Fe Sites: A Highly Active Cathode Catalyst for Alkaline Polymer Electrolyte Fuel Cells, ACS Catal. 7 (2017) 6485–6492. https://doi.org/10.1021/acscatal.7b02340.